Quantum Sensing and Control of Spin-State Dynamics in the Radical-Pair Mechanism

Amit Finkler [1,*] and Durga Dasari [2]

[1] *Department of Chemical and Biological Physics, Weizmann Institute of Science, Rehovot 7610001, Israel*
[2] *3. Physikalisches Institut, Universität Stuttgart, Stuttgart 70569, Germany*

Radical pairs and the dynamics they undergo are prevalent in many chemical and biological systems. Specifically, it has been proposed that the radical-pair mechanism results from a relatively strong hyperfine interaction with its intrinsic nuclear spin environment. While the existence of this mechanism is undisputed, the nanoscale details remain to be experimentally shown. Here, we analyze the role of a quantum sensor in detecting the spin dynamics (non-Markovian) of individual radical pairs in the presence of a weak magnetic field. We show how quantum control methods can be used to set apart the dynamics of the radical-pair mechanism at various stages of the evolution. We expect these findings to have implications to the understanding of the physical mechanism in magnetoreception and other biochemical processes with a microscopic detail.

I. INTRODUCTION

Spin plays a fundamental role in many chemical reactions, from photosynthesis [1] to polymerization [2]. One of the most well studied of those is known as the radical-pair mechanism, or RPM [3]. There, radical pairs are formed of biomolecules with a free electron ($S = 1/2$) that constitute a spin-correlated pair due to electron transfer. Upon collective excitation of these pairs, one could study their dynamics in the collective two-electron spin basis (triplet or singlet) [4]. Due to interaction with an external magnetic field and the existence of hyperfine interaction with the nuclear spins of each radical, this pair of radicals can undergo oscillations between its triplet and singlet states, with a frequency that is mostly dependent on the strength of this hyperfine coupling with respect to the external magnetic field experienced by the radical pair [5]. The RPM has been studied extensively using recombination fluorescence [6], electrochemistry [7], transient electron spin resonance (ESR) [8,9], and ultrafast absorption spectroscopy [10–12]. All of these techniques probe samples of macroscopic scale, namely microliters or 10^{18} molecules. While providing a wealth of information and improving our understanding of some key processes in the said mechanism, the aforementioned tools provide an ensemble average indication as to the magnetic properties that one wants to explore. The RPM is typically characterized by the spin coherence time [13–16] and the recombination rate $\tilde{\kappa}$, i.e., the rate at which the pairs recombine back to their original constituents [17]. Following previous proposals to detect radical-pair dynamics on the single-molecule level [18–20], our approach, using a nanoscale single-spin sensor in the form of the nitrogen-vacancy (N-V) center in diamond [18,21,22], shows that some of the most remarkable features of the RPM are masked by averaging and allows us to probe this territory. Our quantum-sensing technique can assist in determining not only the charge state of the pair [19] but perhaps more importantly, its spin state. We introduce a detection-pulse scheme for single-qubit magnetometry [22–24] that enables a consistent way of realizing whether the pair is in its singlet or one of its three possible triplet states. As this is a single-spin sensor operated in a detection regime where only a small amount of molecules (and hence radical pairs or spins) contribute to the signal [25–27], we also show how quantum control schemes [14] allow us to modify and, in some instances, also enhance the interaction of the radical pair with its external environment, thereby achieving a change in the ratio between the final products.

II. MODEL

We consider a prototypical model used to analyze the sensitivity of a radical-pair (RP) reaction to an external field (ω), wherein a radical pair (σ), composed of two electrons (spin 1/2) is coupled to a nuclear spin environment (I). In addition, we also couple the radical-pair spins to a sensor (spin 1), S. The Hamiltonian describing their dynamics is given by

*amit.finkler@weizmann.ac.il

$$H = h_A \mathbf{I}_A \cdot \boldsymbol{\sigma}_A + h_B \mathbf{I}_B \cdot \boldsymbol{\sigma}_B + \omega(\sigma_A^z + \sigma_B^z) + gS^z(\sigma_A^z + \sigma_B^z), \tag{1}$$

where $h_{A,B}$ are the hyperfine coupling constants and g is the RP-sensor coupling strength. For simplicity, we set $h_B = 0$ and consider a single nuclear spin as the dynamics generated by the above Hamiltonian becomes exactly solvable [28,29]. We would like to note that the simplified sensor-RP interaction is possible due to the large zero-field splitting of the sensor states. Further, the nonsecular interactions, such as $S^z\sigma_{A/B}^x$, could be omitted when $\omega < g$ but could become relevant for $\omega \sim g$. For simplicity, we omit such terms and only focus on the secular interactions shown above. One could choose a two-level subspace spanned either by $|-1\rangle, |0\rangle$ or $|+1\rangle, |0\rangle$ as the computational subspace for the sensor spin. For example, in this basis of the sensor $|\pm 1\rangle, |0\rangle$, the above Hamiltonian can be further simplified to

$$H = H_0 |0\rangle \langle 0| + H_\pm |\pm 1\rangle \langle \pm 1|. \tag{2}$$

Here, $H_0 = h_A \mathbf{I} \cdot \boldsymbol{\sigma}_A + \omega(\sigma_A^z + \sigma_B^z)$ and $H_\pm = h_A \mathbf{I} \cdot \boldsymbol{\sigma}_A + (\omega \pm g)(\sigma_A^z + \sigma_B^z)$. From Eq. 2, it is clear that the coupling to the sensor leads to a modified external field.

A. Dynamics

The singlet-product yield, also known as the singlet fraction [28], $\Phi_S(t)$, quantifies the fraction of radical pairs in the singlet state at time t. Due to the sensor spin-state-dependent enhancement (or reduction) of the effective external field seen by the radical pair, the singlet-product yield Φ_S varies with the occupation probability of the sensor in either of its spin states (see Appendix C). In turn, this leads to a visible contrast in the spin-state readout of the sensor itself. To see this, we evaluate the dynamics governed by the above Hamiltonian. The corresponding time-evolution operator is given by

$$U = U_0 |0\rangle \langle 0| + U_{\pm 1} |\pm 1\rangle \langle \pm 1|, \tag{3}$$

where $U_0 = e^{iH_0 t}$ and $U_{\pm 1} = e^{iH_\pm t}$. Starting from an initial state of the sensor in $|\psi\rangle_S = \frac{1}{\sqrt{2}}[|0\rangle + |1\rangle]$ and of the RP in a singlet state $|\psi\rangle_\sigma = \frac{1}{\sqrt{2}}[|\uparrow\downarrow\rangle - |\downarrow\uparrow\rangle]$, the time-evolved state for the total system can be found using

$$\rho(t) = U\rho(0)U^\dagger, \tag{4}$$

where $\rho(0) = |\psi\rangle_S \langle\psi|_S \otimes |\psi\rangle_\sigma \langle\psi|_\sigma \otimes \frac{1}{2}\hat{I}_A$. We consider an initial thermal state for the nuclear spin, i.e., a fully mixed state $\frac{1}{2}\hat{I}_A$. The reduced state of RP spins and their coupled nuclear spins can be obtained by tracing out the

sensor degrees of freedom and vice versa, respectively, as

$$\rho_{\sigma, I_A}(t) = \text{Tr}_S \rho(t), \quad \rho_S(t) = \text{Tr}_{\sigma, I_A} \rho(t). \tag{5}$$

For the above initial state of the sensor, the RP state is

$$\rho_{\sigma, I_A}(t) = \frac{1}{2}\left[U_0 \rho_{\sigma, I_A}(t) U_0^\dagger + U_{\pm 1}\rho_{\sigma, I_A}(t) U_{\pm 1}^\dagger\right]. \tag{6}$$

Due to the above symmetry, the total singlet fraction will also be $\Phi_S = (\Phi_S^1 + \Phi_S^0)/2$ (see the Appendix C for details). The reduced density matrix of the sensor at time t is simply given by

$$\rho_S(t) = \frac{1}{2}\left[|0\rangle\langle 0| + |1\rangle\langle 1| + C_\Phi(t)|0\rangle\langle 1| + C_\Phi^*(t)|1\rangle\langle 0|\right], \tag{7}$$

where $C_\Phi = \text{Tr}_{\sigma, I_A}\left[U_0(|\psi\rangle_\sigma \langle\psi|_\sigma \otimes \frac{1}{2}\hat{I}_A)U_{\pm 1}^\dagger\right]$ and the trace is bounded by ± 1, and is directly accessible in experiments. The above trace can be further simplified to obtain a closed-form expression given by

$$\begin{aligned}
C_\Phi(t) = \frac{1}{\Omega_1 \Omega_2} \Big\{ &\sin(t\Omega_1)\left[2\left(\Omega_1^2 + g\omega\right)\cos(gt)\sin(t\Omega_2)\right. \\
&\left. - 2\omega\Omega_2 \sin(gt)\cos(t\Omega_2)\right] \\
&+ \Omega_1 \cos(t\Omega_1)\left[2(g+\omega)\sin(gt)\sin(t\Omega_2)\right. \\
&\left. + 2\Omega_2 \cos(gt)\cos(t\Omega_2)\right] + 2\Omega_1\Omega_2 \Big\}, \tag{8}
\end{aligned}$$

where $\Omega_1 = \sqrt{h_A^2 + \omega^2}$ and $\Omega_2 = \sqrt{h_A^2 + (\omega + g)^2}$. This is the central result of the paper and from this we obtain directly the dynamic behavior shown in Fig. 1(b). The singlet recombination rate κ determines how fast the RP state is reset back to the singlet state before a significant hyperfine-driven singlet-to-triplet conversion can take place. Within the Markov approximation, one can include the spin relaxation rate γ of the sensor together with κ, to obtain an effective relaxation rate $\tilde{\kappa} = \kappa + \gamma$. To obtain the steady-state singlet population and further the contrast, we evaluate the expression

$$C_\Phi(\tilde{\kappa}) \approx \tilde{\kappa}\int_0^\infty dt\, C_\phi(t)e^{-\tilde{\kappa}t}, \tag{9}$$

As Eq. 9 simply represents the Laplace transform of several trigonometric functions, it becomes exactly solvable (see the Appendix C). As the coherence time of the sensor is much longer than the singlet recombination rate κ, the asymptotic dependence of both the singlet fraction and the sensor contrast (C_Φ) is hardly affected by the sensor lifetimes. We now use this to perform sensitivity analysis of the sensor with respect to the changes both in the external field (ω) and the coupling strength (g) to the
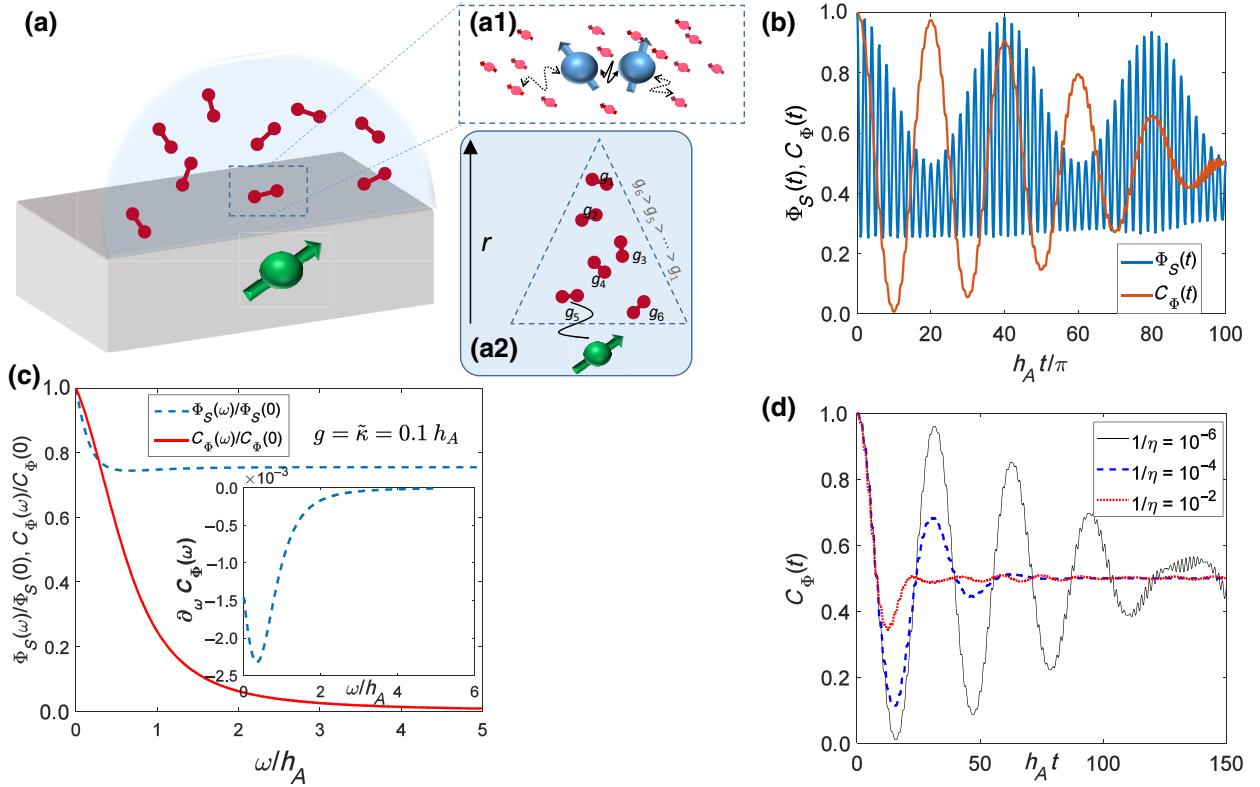
FIG. 1. (a) A schematic representation of the system, wherein the radical-pair spins deposited on the surface of the diamond are sensed and/or controlled by a single spin sensor embedded in a solid-state matrix. Inset (a1) shows the coupling of radical-pair spins to their local nuclear spin environment and in (a2) the distance-dependent coupling of the single-spin sensor to the radical-pair spins. (b) The singlet-triplet oscillations and the corresponding oscillations in the contrast of the sensor are shown as a function of time. (c) The asymptotic singlet-state population [28] and the sensor spin contrast [Eq. (C4)] are plotted as a function of a weak external field ω. In the inset, we show the low-field effect for the sensor contrast (black dotted line), where we plot the first derivative of the contrast C_Φ. (d) The average contrast C_Φ obtained from an ensemble of RPs and the couplings described by a distribution as shown in Eq. (10). Here, we show the contrast obtained from a single (black line) to an ensemble of RPs (blue dashed, red dotted) characterized by the parameter η. In the above simulations, we choose all the parameters in units of the hyperfine coupling strength h_A: the singlet recombination rate $\tilde{\kappa} = 0.01 h_A$ [shown in (b) and (d)] and the sensor-RP coupling to be $g = 0.1 h_A$. In (b)–(d), all x-axis units are dimensionless and all y-axis units are either normalized (and hence unitless) or constitute a derivative of the latter.

RP. In Fig. 1(c) we show the effect of the magnetic field (ω) on the singlet yield of a one-proton radical pair [see Eq. (1)]. It has been shown previously that the singlet-product yield shows an abrupt change even due to a tiny magnetic field in the low-field limit and for a slow recombination rate κ [16,30]. Similar behavior is observed in the case of sensor contrast, C_Φ, where for $\omega/h_A \ll 1$, the change in the contrast ($\partial_\omega C_\Phi$) is large, while for large fields ($\omega \gg g$) it vanishes. The singlet fraction shown here is the steady-state population obtained in the long-time limit, but nevertheless one could also analyze the dynamics for times shorter than the relaxation time, as shown in Fig. 1(b). The effects of singlet-triplet oscillations are also seen on the sensor contrast. As opposed to the fast oscillations in the singlet fraction caused by the hyperfine interaction h_A, the oscillation frequency of the sensor contrast is due to the small coupling strength $g \ll h_A$.

III. ENSEMBLE SENSING

While the above analysis holds for a single RP with a given interaction strength g to the sensor, in general, in a practical setting, an ensemble of RPs is drop casted on top of the sensor surface or on the apex of an AFM tip and then scanned with respect to the sensor [31]. Due to this, the sensor interacts with a large number of RPs within a sensing volume that is determined by the distance between the surface and the sensor [32]. Owing to interaction with a large number of RPs, both the singlet production rate and the sensor contrast become affected due to the averaging over the effective field generated by the sensor on the different RPs and vice versa. Such effective fields produced by an RP spin bath could be approximated in the quasistatic approximation by a Gaussian distribution [33] when the effective field produced by the bath is varying slowly in time. Upon using such a distribution for g, one

can integrate the functions given in Eq. (8), as

$$\Phi_S(\eta) \sim C_0 \int dg e^{-\eta(g-g_0)^2} \Phi_S(g),$$

$$C_\Phi(\eta) \sim C_0 \int dg e^{-\eta(g-g_0)^2} C_\Phi(g),$$

(10)

where the normalization constant $C_0 = \sqrt{\pi} \left[\mathrm{erf}\left(\sqrt{\eta}g_0\right) + 1 \right] / 2\sqrt{\eta}$, and erf(x) is the error function. For an increasing width of this distribution, the oscillations seen in the single-RP limit eventually vanish in the large-N limit. Similar behavior can also be seen for a finite time in Fig. 1(b), where we directly plot the time-dependent behavior of the triplet-pair production $\Phi(t)$ from the unitary evolution generated by the Hamiltonian given in Eq. (1). The characteristic oscillations of the triplet fraction shown in Fig. 1(d) indicate the singlet-triplet oscillations. In the presence of interaction with the sensor, the dampening of the oscillations can be understood as an additional random phase ϕ (see the Appendix C) introduced by the sensor coupling, leading to a gradual loss of coherent behavior of the triplet-pair production in time. As shown in Fig. 2, this can be overcome by employing a high-strength magnetic field gradient [26] on an atomic force microscope (AFM) tip, which has been experimentally achieved by several groups [26,34,35]. Both the asymptotic and the finite-time analysis clearly display the role of an additional sensor interaction both for sensing the RP dynamics and, in turn, influencing its production rate. This influence can be further induced in a controlled manner if one employs coherent control of the sensor spin (see the Appendix D).

IV. EXPERIMENTAL IMPLEMENTATION

Apart from the theoretical model shown here, we also propose an apparatus for sensing and controlling the RP spin state as described above. This consists of a scanning confocal microscope for the initialization and readout of a single N-V center in diamond [21,23,36]. A green laser (520 nm) is used for excitation and the N-V fluorescence in the range of 650–800 nm is collected and focused onto an avalanche photodiode. The microscope is integrated with a variable magnetic field implemented by either a permanent magnet (Nd-Fe-B or Sm-Co) on an *XYZ* stage for a room-temperature setup or a set of three pairs of split Helmholtz coils for a low-temperature measurement. In addition, a microwave antenna is positioned near the N-V center for spin-state manipulation of both the N-V spin and the RP state. A schematic of such an apparatus is shown in Fig. 2(a). A solution containing a dilute amount of precursor molecules can be drop casted on the surface of a diamond containing shallow N-V centers. Protection of the molecules from denaturation can be achieved by encapsulation in a polymer matrix [37]. Yet another method is diamond-surface functionalization [38], which will create covalent bonds between the functional groups on the diamond and the molecules. For such sensors, situated approximately 5–10 nm below the surface of the diamond [39], the typical decoherence time (spin echo) is $T_2 \sim 10 - 20 \,\mu$s, allowing for an ac-magnetic-field sensitivity of a few nT/Hz$^{1/2}$ [22,40]. Finally, we take RPs based on the Flavin-Tryptophan pair in cryptochrome as a widely studied example [8,41], where a pulsed blue laser diode (460 nm) can be used to excite RPs. Short (10-ns) pulses are sufficient to create RPs in cryptochrome [8] and
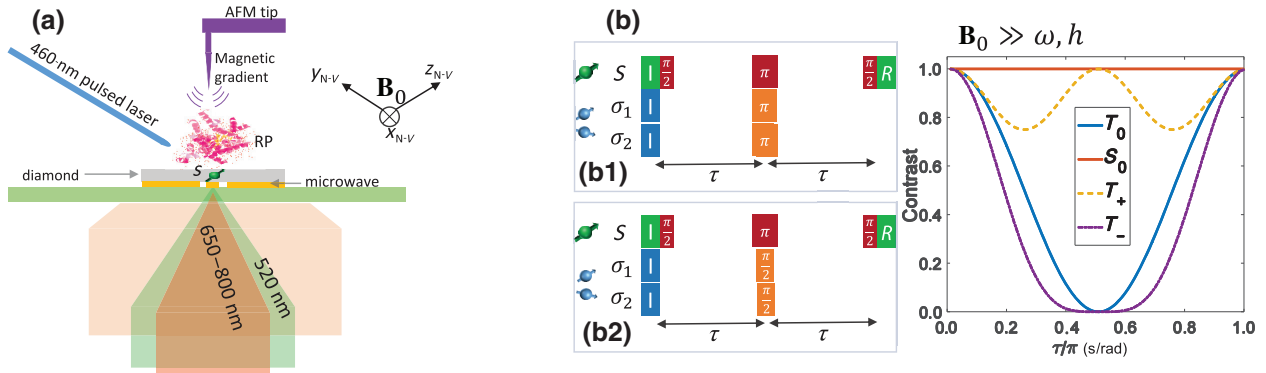

FIG. 2. (a) A schematic representation of the experimental setup, displaying a diamond substrate with precursor molecules, where the RPM is photoexcited, on its surface. We also show the initialization and readout mechanism of the sensor spin (N-V) state through the green laser (520 nm) and detection through its red side-band emission (650–800 nm). A blue LED (460 nm) is used to initialize the RP mechanism that will be sensed through the N-V center in the diamond lattice. $\mathbf{B}_0$ is an externally applied magnetic field aligned with the N-V axis so as to maximize the N-V readout and tune the local magnetic field. A high-strength magnetic field gradient is placed on an AFM tip, effecting a local spectral and hence spatial separation between the radical pairs. (b) We show the modified double electron-electron resonance (DEER) pulse sequence (b_1) in b_2 wherein a π pulse is replaced by a $\pi/2$ pulse to differentiate the singlet and triplet states, as shown in the plot on the right, where we vary the free evolution time τ and initialize the RP in various spin states. In (b), the y-axis units are normalized (and hence unitless).

hence are short enough so as not to interfere with our proposed sensing protocol. This wavelength has been shown to be efficient in creating RPs in this makeup. Not only that, but the absorption spectrum of cryptochrome is coincidentally "orthogonal" to that of the N-V center [8,42], preventing optical signal quenching, which might reduce the SNR. Furthermore, the N-V spin resonance is shifted by 2.87 GHz with respect to that of a free electron due to zero-field splitting [43], which allows for selective addressing and manipulation of the N-V spin independent of the RP state and vice versa. Spin relaxation times for this RP system are estimated to be in the range of a few microseconds, consistent with transient absorption experiments [30] and also viable for the shallow N-V center mentioned above [27,37]. For a realistic N-V ac-magnetic-field sensitivity of 10 nT/Hz$^{1/2}$ and a distance of 20 nm between the N-V and the RP, we expect to be able to achieve an SNR of 1 after a measurement time of 10 s [22,40]. As each iteration of our pulse sequence is on the order of 10 μs, and with a single-shot SNR 0.03 (for a single readout pulse), each data point in the scheme proposed above [see Fig. 2(b)] needs at least 10^5 repetitions, or 1 s, to achieve an SNR of 10 [44]. When taking extra measures for canceling sources of noise [45], considering the reduced contrast (and hence, SNR) in nested N-V magnetometry measurements [32,46] and utilizing quantum-assisted methods to improve the readout efficiency [47–49], a full data set would be acquired in about 1 h, after accounting for the full photocycle relaxation between subsequent measurements [16,50]. See the Appendix B for a more detailed calculation.

V. QUANTUM CONTROL

As both the sensor and the target spins are electrons, one can simultaneously manipulate the sensor and target spins similar to the DEER experiments known in ESR. Additionally, here, as we have two target electron spins, one can employ a triple electron-electron resonance (TEER) sequence as an alternative method to detect the spin state of the radical pair. We have introduced and experimentally verified such multielectron resonance control earlier, in Ref. [27]. This entails a preliminary frequency scan of the Larmor precession frequency of each radical, taking into account a small (zero) shift between the two radicals in the pair due to direct dipole-dipole interactions ($\boldsymbol{\sigma}_A \cdot \mathbf{J} \cdot \boldsymbol{\sigma}_B$), which we do not consider in our calculations here. Combining this with the proposed protocol for the charge-state determination of the pair [19], our spin-state scheme can allow us to distinguish between the different triplet spin states, as well as giving a threshold below which we can safely establish that the RP is in the singlet state. In Fig. 2(b) we show the original and modified TEER pulse sequences for detecting the exact spin state of the RP. In Fig. 2(b) the normalized contrast of the N-V center when employing this pulse sequence while varying

the time between microwave pulses, τ, is shown and the four spin states of the two-electron system (RP) become clearly distinguishable. The N-V decoherence time and RP spin relaxation time are both in the relevant range for such TEER sensing [27].

The experimental difficulty in clearly resolving the singlet-triplet oscillations stems from the ensemble dynamics of the RP spins in the presence of external field, as shown in Fig. 1(d). One can also use the dynamical control pulses on the sensor spin to resolve its coupling to individual RPs. For this, we choose the computational basis for the sensor spin as $|-1\rangle$, $|0\rangle$. Due to this, the effective field seen by a given RP is $\omega - g$. By scanning the external field ω, one finds an enhanced singlet fraction when the total effective field becomes zero, i.e., the singlet fraction Φ_S peaks at the external field, with an uncertainty (width) determined by the recombination rate $\tilde{\kappa}$. The aspect of quantum control here arises when one periodically changes the spin state of the sensor from $m_s = +1$ to $m_s = -1$ in a controllable way.

VI. CONCLUSION AND OUTLOOK

The use of a quantum sensor—i.e., a true two-level system—as the detection tool opens up a wide range of possibilities for optimization and control that are not accessible to macroscopic or classic objects. Namely, it allows us to decouple the target spin from its surrounding spin bath and even make use of potentially helpful nuclear spins in the immediate vicinity of the radicals, such as those which are hyperfine coupled to them. We find that even such a basic protocol (before optimization) can lead to a visible enhancement of the triplet-to-singlet ratio and hence, in effect, we show control over at least one stage of the RPM. Moreover, due to the quantum nature of both the N-V and the RP, it is possible to devise a model that takes such a single spin sensor and an N-sized collection of RPs and show that as one reduces the number of pairs in the vicinity of the sensor, one can obtain a significantly improved visibility contrast for reading out the state of the pairs.

To conclude, we show here the role of a quantum sensor in sensing and controlling the RP mechanism to weak external fields, both for the case of single and ensemble RPs. We also give modified multi-electron-electron resonance spectroscopy pulse sequences to clearly distinguish the four different singlet or triplet configurations and find the conditions for the optimal sensitivity in terms of the magnetic field strength, the hyperfine interaction, and the recombination rate. We also show a preliminary quantum control aspect wherein modulation of the sensor spin state can have a dramatic effect on the RP dynamics and we envisage that additional tailor-made protocols can improve this even further. Our results continue a line of theoretical proposals for detecting various aspects of the phenomenon

known as the radical-pair mechanism, which can now be considered for experimental realization as the technical aspects of assembling the appropriate setups are being constantly tackled and resolved.

APPENDIX A: ESTIMATION FOR THE MAGNETIC FIELD OF A RADICAL PAIR

The magnetic field from the radical pair is assumed to behave like a magnetic dipole,

$$\mathbf{B} = \frac{\mu_0}{4\pi}\left[\frac{3\mathbf{r}\,(\mathbf{m}\cdot\mathbf{r})}{r^5} - \frac{\mathbf{m}}{r^3}\right],$$

and so for a best-case scenario (where the angle between $\mathbf{m}$ and $\mathbf{r}$ is $\pi/2$), the magnetic field of an electron at a distance of 20 nm is 59 nT.

APPENDIX B: SIGNAL-TO-NOISE CALCULATION

Here, we provide a calculation for the expected time it would take to acquire a full data set of 30 points needed to plot Fig. 1(d). As mentioned in the main text, with standard N-V readout [22], 10^5 repetitions of the pulse sequence are needed for an SNR of 10. The pulse sequence we propose, including laser initialization and readout, is 10 μs long and so together a single data point takes 1 s to acquire. The DEER and TEER protocols assume a reduced contrast of 4% and 0.5%, respectively [27], leading to a stretching of each data-point acquisition to 8.5 and 70 s, respectively [50]. Therefore, a data set of 30 points is expected to take 2100 s to acquire. This is all under the assumption of a relatively (μs) short relaxation time of the radical pair [8]. For completeness, we note that if a full re-equilibration of the photocycle is necessary, then the overhead will be 3 orders of magnitude larger [16] and, correspondingly, so will the acquisition time. Nevertheless, with measurements involving a long relaxation time, it is possible to compensate for the relatively poor N-V readout efficiency by using nuclear-spin-assisted single-shot readout [47] and spin-to-charge conversion [48]. Using only the former in combination with an improved photon-collection efficiency [49], we have previously shown [50] how the acquisition time can be reduced by a factor of approximately 400. This would allow us to retain the approximately 1-h acquisition time for a full data set.

Other spurious noise effects that may arise when sensing molecules are, for example, the extraordinary broadening of the hyperfine-coupling (hfc) spectrum seen by the radical pairs due to Jahn-Teller (JT) distortion. Moreover, hfc broadening due to the JT effect in molecules is rarely seen in radical pairs and typically requires octohedral symmetry or a similar one; for example, a prolate fullerene.

While many such possible interactions, especially the complex ones, cannot be modeled in totality, the current literature suggests that all such effects lead to an effectively modified field distribution sensed by the N-V center, which should eventually lead to an effective reduction in the spin relaxation (T_1) and spin coherence (T_2) times of the N-V center. In typical N-V experiments, candidate N-V centers in the diamond are characterized before application of the molecules, which allows for quantifying their T_1 and T_2 properties and even their magnetic noise spectrum [51]. Therefore, separation of the noise effects arising from the internal and external sources could be well quantified.

APPENDIX C: TRIPLET FRACTION

Based on the one-proton radical-pair model presented in Ref. [28], we calculate $\Phi_T(t) = 1 - \Phi_S(t)$, where

$$\begin{aligned}
\Phi_S^g(t) &= \frac{3}{8} + \frac{1}{8}\frac{(\omega+g)^2}{\Omega^2} + \frac{1}{8}\frac{h^2}{\Omega^2}f\,(\Omega) \\
&+ \frac{1}{8}\left[1 - \frac{(\omega+g)}{\Omega}\right]f\left(\frac{1}{2}h + \frac{1}{2}(\omega+g) + \frac{1}{2}\Omega\right) \\
&+ \frac{1}{8}\left[1 - \frac{(\omega+g)}{\Omega}\right]f\left(\frac{1}{2}h - \frac{1}{2}(\omega+g) - \frac{1}{2}\Omega\right) \\
&+ \frac{1}{8}\left[1 + \frac{(\omega+g)}{\Omega}\right]f\left(\frac{1}{2}h - \frac{1}{2}(\omega+g) + \frac{1}{2}\Omega\right) \\
&+ \frac{1}{8}\left[1 + \frac{(\omega+g)}{\Omega}\right]f\left(\frac{1}{2}h + \frac{1}{2}(\omega+g) - \frac{1}{2}\Omega\right).
\end{aligned}$$

Here, h is the hyperfine coupling strength in rad/s, ω is the Zeeman interaction term or magnetic field in rad/s, $\omega = 2\gamma B$, $\Omega = \sqrt{h^2 + (\omega+g)^2}$, and

$$f\,(x) = \cos(xt + \varphi). \tag{C1}$$

Note that φ is not included in the original derivation and accounts for a random phase for each radical pair. For the case of a single spin sensor this phase is crucial, since indeed each radical pair has a different distance and solid angle relative to the sensor. We take a magnetic field of 50 μT and a hyperfine interaction strength of 14 MHz. One can also see the back action of the sensor on the RP dynamics, where the effective field is now $(\omega+g)$ instead of ω.

For example, if $\omega = g$, and the N-V sensor is in the spin state $|-1\rangle$, then the effective seen by the RP is zero and the singlet fraction jumps suddenly when scanning the field strength.

We consider a radical pair initially formed in a singlet configuration and evolving under both the hyperfine interaction with its neighboring nuclear spins and with the external (Zeeman) field. For the current discussion, we neglect their intraspin interaction and consider their interaction with a nearby probe spin, the N-V center. From the coherent evolution of the pair $\rho(t)$, the singlet-state dynamics can be evaluated as

$$P_S(t) = [|S_0\rangle\langle\rho(t)|], \qquad (C2)$$

where $\rho(t)$ is obtained by tracing out the degrees of freedom of the nuclear and probe spins. Further, upon considering the radical-pair recombination mechanisms, the decay of the singlet products, or the singlet yield in the RP mechanism, is simply captured through

$$\mathcal{P}_S(\kappa) = \int_0^t dt P_S(t) e^{-\kappa t}. \qquad (C3)$$

Similarly, the contrast as defined in Eq. (9) can be evaluated to yield an exact expression as follows:

$$
\begin{aligned}
C_\Phi(\tilde\kappa) = 1/2 - \frac{1}{4}\tilde\kappa \Bigg[& \frac{\left[\omega(g+\omega)+h_A^2\right]\left(-\frac{\tilde\kappa}{2[\tilde\kappa^2+(g+\Omega_1+\Omega_2)^2]} - \frac{\tilde\kappa}{2[\tilde\kappa^2+(-g+\Omega_1+\Omega_2)^2]} + \frac{\tilde\kappa}{2[\tilde\kappa^2+(g-\Omega_1+\Omega_2)^2]} + \frac{\tilde\kappa}{2[\tilde\kappa^2+(g+\Omega_1-\Omega_2)^2]}\right)}{\Omega_1\Omega_2} \\
& + \frac{(g+\omega)\left(\frac{\tilde\kappa}{2[\tilde\kappa^2+(-g+\Omega_1+\Omega_2)^2]} - \frac{\tilde\kappa}{2[\tilde\kappa^2+(g+\Omega_1+\Omega_2)^2]}\right)}{\Omega_2} \\
& + \frac{\omega\left(\frac{\tilde\kappa}{2[\tilde\kappa^2+(g+\Omega_1+\Omega_2)^2]} - \frac{\tilde\kappa}{2[\tilde\kappa^2+(-g+\Omega_1+\Omega_2)^2]} - \frac{\tilde\kappa}{2[\tilde\kappa^2+(g-\Omega_1+\Omega_2)^2]} + \frac{\tilde\kappa}{2[\tilde\kappa^2+(g+\Omega_1-\Omega_2)^2]}\right)}{\Omega_1} \\
& + \left(\frac{\tilde\kappa}{2\left[\tilde\kappa^2+(g+\Omega_1+\Omega_2)^2\right]} + \frac{\tilde\kappa}{2\left[\tilde\kappa^2+(-g+\Omega_1+\Omega_2)^2\right]} + \frac{\tilde\kappa}{2\left[\tilde\kappa^2+(g-\Omega_1+\Omega_2)^2\right]}\right. \\
& \left. + \frac{\tilde\kappa}{2\left[\tilde\kappa^2+(g+\Omega_1-\Omega_2)^2\right]}\right) + \left(\frac{\tilde\kappa}{2\left[\tilde\kappa^2+(g+\Omega_1-\Omega_2)^2\right]} - \frac{\tilde\kappa}{2\left[\tilde\kappa^2+(g-\Omega_1+\Omega_2)^2\right]}\right)\Bigg],
\end{aligned} \qquad (C4)
$$

where $\Omega_1 = \sqrt{\omega^2 + h_A^2}$ and $\Omega_2 = \sqrt{(\omega+g)^2 + h_A^2}$.

APPENDIX D: QUANTUM CONTROL

The ability to control the singlet-product yield through the quantum sensor becomes possible due to the sensor spin-state-dependent evolution of the radical pair. Upon coherent flipping of the sensor spin, the singlet yield can be manipulated and hence its sensitivity to low fields and low recombination rates. To see this, we write down the evolution operator corresponding to the above Hamiltonian, given by

$$U = U_0 |0\rangle\langle 0| + U_1 |1\rangle\langle 1|. \qquad (D1)$$

Let us consider a π-flip operation on the sensor spin, followed by the time evolution. This leads to a modified time-evolution operator, given by

$$V_1 = Ue^{i\pi S^x}U = U_1 U_0 |1\rangle\langle 0| + U_0 U_1 |0\rangle\langle 1|. \qquad (D2)$$

Upon the application of M (even) π pulses, the final evolution operator takes the simple form

$$
\begin{aligned}
V_M = U\cdots e^{i\pi S^x}Ue^{i\pi S^x}U &= (U_1U_0)^{M/2}|1\rangle\langle 0| \\
&+ (U_0U_1)^{M/2}|0\rangle\langle 1|.
\end{aligned} \qquad (D3)
$$

From the above evolution, the singlet yield is additionally dependent on the stroboscopic interruptions of the evolution for every time τ.

APPENDIX E: LOW-FIELD CONTROL

For measuring fields on the order of Earth's magnetic field, we harness the degeneracy of the $|\pm 1\rangle$ states of the sensor at zero field. The $|\pm 1\rangle$ states are never ideally degenerate due to a finite splitting caused by the Earth's magnetic field. To cancel this, one should apply an external field in the opposite direction. At this degeneracy point, one could drive a microwave transition $|0\rangle \leftrightarrow$

$\frac{1}{\sqrt{2}}[|+1\rangle + |-1\rangle]$ at exactly the zero-field splitting of the sensor, i.e., $D = 2.87$ GHz. This technique is commonly used for quantum control in quantum communication protocols, developed by one of us previously in [52] and widely explored in the N-V community (cf. Ref. [53]). For such measurements, one would use the $|\pm 1\rangle$ states of the sensor instead of $|0\rangle, |1\rangle$ employed here. The sensitivity to the RP dynamics has a twofold enhancement in this basis. Furthermore, at low temperature one could harness the single-shot readout of the electron spin for such measurements, to obtain a further improvement in the SNR [54].

APPENDIX F: GRADIENT

A gradient tip allows for an on-demand application of a magnetic field with a gradient of 1 G/nm, or 2.8 MHz per nanometer for electron spins with $g = 2$, as is the case of the radical pairs that we are discussing. This means that any RP that is not within a 1 nm radius of the RPs under investigation will be completely decoupled from it, since its resonant frequency will be shifted by several megahertz from that of the RPs. To effect such a change in the magnetic field, there is in fact no need for a high absolute value of the *magnetic field* but, rather, only a high *gradient*. Since the magnetic field gradient created by the AFM tip is a crucial component of the experimental implementation, in Fig. 3 we provide a result of a short numerical calculation using finite-element analysis, assuming a magnetized nickel apex with a diameter of 30 nm deposited on a quartz tip. The AFM tip is assumed to be at a height of 40 nm above the surface of the diamond.
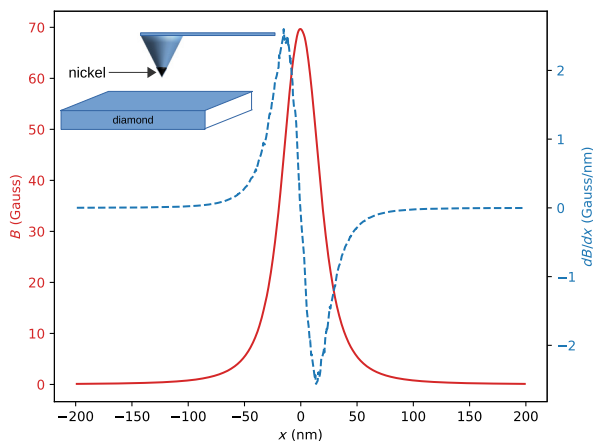

FIG. 3. A numerical calculation by finite-element analysis of the magnetic field, B, effected by a magnetic AFM tip, assuming a 30-nm layer of nickel deposited on a quartz tip, brought to a distance of 40 nm from the surface of the diamond. The plot shows the magnetic field profile (red solid line) and the spatial derivative dB/dx (blue dashed line) as a function of the position under the center of the tip, x.

The calculation shows that one can find different positions away from the center of the tip where the absolute magnetic field is 12 G but the gradient is already at 1 G/nm.

[1] J. R. Norris, R. A. Uphaus, H. L. Crespi, and J. J. Katz, Electron spin resonance of chlorophyll and the origin of signal I in photosynthesis, Proc. Natl. Acad. Sci. **68,** 625 (1971).

[2] B. Yamada, D. G. Westmoreland, S. Kobatake, and O. Konosu, ESR spectroscopic studies of radical polymerization, Prog. Polym. Sci. **24,** 565 (1999).

[3] U. E. Steiner and T. Ulrich, Magnetic field effects in chemical kinetics and related phenomena, Chem. Rev. **89,** 51 (1989).

[4] R. Kaptein and J. Oosterhoff, Chemically induced dynamic nuclear polarization II: (Relation with anomalous ESR spectra), Chem. Phys. Lett. **4,** 195 (1969).

[5] O. Anisimov, V. Bizyaev, N. Lukzen, V. Grigoryants, and Y. Molin, The induction of quantum beats by hyperfine interactions in radical-ion pair recombination, Chem. Phys. Lett. **101,** 131 (1983).

[6] D. Stass, J. Woodward, C. Timmel, P. Hore, and K. McLauchlan, Radiofrequency magnetic field effects on chemical reaction yields, Chem. Phys. Lett. **329,** 15 (2000).

[7] Z. Zeng, J. Wei, Y. Liu, W. Zhang, and T. Mabe, Magnetoreception of photoactivated cryptochrome 1 in electrochemistry and electron transfer, ACS Omega **3,** 4752 (2018).

[8] T. Biskup, E. Schleicher, A. Okafuji, G. Link, K. Hitomi, E. Getzoff, and S. Weber, Direct observation of a photoinduced radical pair in a cryptochrome blue-light photoreceptor, Angew. Chem. Int. Ed. **48,** 404 (2009).

[9] S. Weber, T. Biskup, A. Okafuji, A. R. Marino, T. Berthold, G. Link, K. Hitomi, E. D. Getzoff, E. Schleicher, and J. R. Norris, Origin of light-induced spin-correlated radical pairs in cryptochrome, J. Phys. Chem. B **114,** 14745 (2010).

[10] M. Liedvogel, K. Maeda, K. Henbest, E. Schleicher, T. Simon, C. R. Timmel, P. J. Hore, and H. Mouritsen, Chemical magnetoreception: Bird cryptochrome 1a is excited by blue light and forms long-lived radical-pairs, PLoS ONE **2,** e1106 (2007).

[11] K. Maeda, K. B. Henbest, F. Cintolesi, I. Kuprov, C. T. Rodgers, P. A. Liddell, D. Gust, C. R. Timmel, and P. J. Hore, Chemical compass model of avian magnetoreception, Nature **453,** 387 (2008).

[12] C. Kerpal, S. Richert, J. G. Storey, S. Pillai, P. A. Liddell, D. Gust, S. R. Mackenzie, P. J. Hore, and C. R. Timmel, Chemical compass behaviour at microtesla magnetic fields strengthens the radical pair hypothesis of avian magnetoreception, Nat. Commun. **10,** 3707 (2019).

[13] I. K. Kominis, Quantum Zeno effect explains magnetic-sensitive radical-ion-pair reactions, Phys. Rev. E **80,** 056115 (2009).

[14] J. Cai, G. G. Guerreschi, and H. J. Briegel, Quantum Control and Entanglement in a Chemical Compass, Phys. Rev. Lett. **104,** 220502 (2010).

[15] E. M. Gauger, E. Rieper, J. J. L. Morton, S. C. Benjamin, and V. Vedral, Sustained Quantum Coherence and

Entanglement in the Avian Compass, Phys. Rev. Lett. **106,** 040503 (2011).

[16] D. R. Kattnig, J. K. Sowa, I. A. Solov'yov, and P. J. Hore, Electron spin relaxation can enhance the performance of a cryptochrome-based magnetic compass sensor, New J. Phys. **18,** 063007 (2016).

[17] C. T. Rodgers and P. J. Hore, Chemical magnetoreception in birds: The radical pair mechanism, Proc. Natl. Acad. Sci. **106,** 353 (2009).

[18] J. Cai, F. Jelezko, M. B. Plenio, and A. Retzker, Diamond-based single-molecule magnetic resonance spectroscopy, New J. Phys. **15,** 013020 (2013).

[19] H. Liu, M. B. Plenio, and J. Cai, Scheme for Detection of Single-Molecule Radical Pair Reaction Using Spin in Diamond, Phys. Rev. Lett. **118,** 200402 (2017).

[20] N. Ikeya, E. A. Nasibulov, K. L. Ivanov, K. Maeda, and J. R. Woodward, Single-molecule spectroscopy of radical pairs: A theoretical treatment and experimental considerations, Mol. Phys. **117,** 2604 (2018).

[21] A. Gruber, A. Dräbenstedt, C. Tietz, L. Fleury, J. Wrachtrup, and C. v. Borczyskowski, Scanning confocal optical microscopy and magnetic resonance on single defect centers, Science **276,** 2012 (1997).

[22] J. M. Taylor, P. Cappellaro, L. Childress, L. Jiang, D. Budker, P. R. Hemmer, A. Yacoby, R. Walsworth, and M. D. Lukin, High-sensitivity diamond magnetometer with nanoscale resolution, Nat. Phys. **4,** 810 (2008).

[23] G. Balasubramanian, I. Y. Chan, R. Kolesov, M. Al-Hmoud, J. Tisler, C. Shin, C. Kim, A. Wojcik, P. R. Hemmer, A. Krueger, T. Hanke, A. Leitenstorfer, R. Bratschitsch, F. Jelezko, and J. Wrachtrup, Nanoscale imaging magnetometry with diamond spins under ambient conditions, Nature **455,** 648 (2008).

[24] J. R. Maze, P. L. Stanwix, J. S. Hodges, S. Hong, J. M. Taylor, P. Cappellaro, L. Jiang, M. V. G. Dutt, E. Togan, A. S. Zibrov, A. Yacoby, R. L. Walsworth, and M. D. Lukin, Nanoscale magnetic sensing with an individual electronic spin in diamond, Nature **455,** 644 (2008).

[25] B. Grotz, J. Beck, P. Neumann, B. Naydenov, R. Reuter, F. Reinhard, F. Jelezko, J. Wrachtrup, D. Schweinfurth, B. Sarkar, and P. Hemmer, Sensing external spins with nitrogen-vacancy diamond, New J. Phys. **13,** 055004 (2011).

[26] M. S. Grinolds, M. Warner, K. D. Greve, Y. Dovzhenko, L. Thiel, R. L. Walsworth, S. Hong, P. Maletinsky, and A. Yacoby, Subnanometre resolution in three-dimensional magnetic resonance imaging of individual dark spins, Nat. Nanotechnol. **9,** 279 (2014).

[27] L. Schlipf, T. Oeckinghaus, K. Xu, D. B. R. Dasari, A. Zappe, F. F. de Oliveira, B. Kern, M. Azarkh, M. Drescher, M. Ternes, K. Kern, J. Wrachtup, and A. Finkler, Molecular quantum spin network controlled by a single qubit, Sci. Adv. **3,** e1701116 (2017).

[28] C. Timmel, U. Till, B. Brocklehurst, K. Mclauchlan, and P. Hore, Effects of weak magnetic fields on free radical recombination reactions, Mol. Phys. **95,** 71 (1998).

[29] H. J. Hogben, T. Biskup, and P. J. Hore, Entanglement and Sources of Magnetic Anisotropy in Radical Pair-Based Avian Magnetoreceptors, Phys. Rev. Lett. **109,** 220501 (2012).

[30] K. Maeda, A. J. Robinson, K. B. Henbest, H. J. Hogben, T. Biskup, M. Ahmad, E. Schleicher, S. Weber, C. R. Timmel, and P. J. Hore, Magnetically sensitive light-induced reactions in cryptochrome are consistent with its proposed role as a magnetoreceptor, Proc. Natl. Acad. Sci. **109,** 4774 (2012).

[31] D. Schmid-Lorch, T. Häberle, F. Reinhard, A. Zappe, M. Slota, L. Bogani, A. Finkler, and J. Wrachtrup, Relaxometry and dephasing imaging of superparamagnetic magnetite nanoparticles using a single qubit, Nano Lett. **15,** 4942 (2015).

[32] T. Staudacher, F. Shi, S. Pezzagna, J. Meijer, J. Du, C. A. Meriles, F. Reinhard, and J. Wrachtrup, Nuclear magnetic resonance spectroscopy on a (5-nanometer)^3 sample volume, Science **339,** 561 (2013).

[33] N. V. Prokof'ev and P. C. E. Stamp, Theory of the spin bath, Rep. Prog. Phys. **63,** 669 (2000).

[34] H. J. Mamin, C. T. Rettner, M. H. Sherwood, L. Gao, and D. Rugar, High field-gradient dysprosium tips for magnetic resonance force microscopy, Appl. Phys. Lett. **100,** 013102 (2012).

[35] T. Oeckinghaus, S. A. Momenzadeh, P. Scheiger, T. Shalomayeva, A. Finkler, D. Dasari, R. Stöhr, and J. Wrachtrup, Spin–phonon interfaces in coupled nanomechanical cantilevers, Nano Lett. **20,** 463 (2019).

[36] F. Jelezko, T. Gaebel, I. Popa, A. Gruber, and J. Wrachtrup, Observation of Coherent Oscillations in a Single Electron Spin, Phys. Rev. Lett. **92,** 076401 (2004).

[37] F. Shi, Q. Zhang, P. Wang, H. Sun, J. Wang, X. Rong, M. Chen, C. Ju, F. Reinhard, H. Chen, J. Wrachtrup, J. Wang, and J. Du, Single-protein spin resonance spectroscopy under ambient conditions, Science **347,** 1135 (2015).

[38] J. Neburkova, J. Vavra, and P. Cígler, Coating nanodiamonds with biocompatible shells for applications in biology and medicine, Curr. Opin. Solid State Mater. Sci. **21,** 43 (2017), nanodiamond Science and Technology.

[39] F. Fávaro de Oliveira, D. Antonov, Y. Wang, P. Neumann, S. A. Momenzadeh, T. Häußermann, A. Pasquarelli, A. Denisenko, and J. Wrachtrup, Tailoring spin defects in diamond by lattice charging, Nat. Commun. **8,** 15409 (2017).

[40] M. S. Grinolds, S. Hong, P. Maletinsky, L. Luan, M. D. Lukin, R. L. Walsworth, and A. Yacoby, Nanoscale magnetic imaging of a single electron spin under ambient conditions, Nat. Phys. **9,** 215 (2013).

[41] C. Bialas, L. E. Jarocha, K. B. Henbest, T. M. Zollitsch, G. Kodali, C. R. Timmel, S. R. Mackenzie, P. L. Dutton, C. C. Moser, and P. J. Hore, Engineering an artificial flavoprotein magnetosensor, J. Am. Chem. Soc. **138,** 16584 (2016).

[42] S.-H. Song, B. Dick, A. Penzkofer, R. Pokorny, A. Batschauer, and L.-O. Essen, Absorption and fluorescence spectroscopic characterization of cryptochrome 3 from Arabidopsis thaliana, J. Photochem. Photobiol., B **85,** 1 (2006).

[43] E. van Oort and M. Glasbeek, Cross-relaxation dynamics of optically excited N-V centers in diamond, Phys. Rev. B **40,** 6509 (1989).

[44] D. Hopper, H. Shulevitz, and L. Bassett, Spin readout techniques of the nitrogen-vacancy center in diamond, Micromachines **9,** 437 (2018).

[45] T. Häberle, D. Schmid-Lorch, F. Reinhard, and J. Wrachtrup, Nanoscale nuclear magnetic imaging with chemical contrast, Nat. Nanotechnol. **10,** 125 (2015).

[46] D. R. Glenn, D. B. Bucher, J. Lee, M. D. Lukin, H. Park, and R. L. Walsworth, High-resolution magnetic resonance spectroscopy using a solid-state spin sensor, Nature **555,** 351 (2018).

[47] P. Neumann, J. Beck, M. Steiner, F. Rempp, H. Fedder, P. R. Hemmer, J. Wrachtrup, and F. Jelezko, Single-shot readout of a single nuclear spin, Science **329,** 542 (2010).

[48] B. J. Shields, Q. P. Unterreithmeier, N. P. de Leon, H. Park, and M. D. Lukin, Efficient Readout of a Single Spin State in Diamond via Spin-to-Charge Conversion, Phys. Rev. Lett. **114,** 136402 (2015).

[49] S. A. Momenzadeh, R. J. Stöhr, F. F. de Oliveira, A. Brunner, A. Denisenko, S. Yang, F. Reinhard, and J. Wrachtrup, Nanoengineered diamond waveguide as a robust bright platform for nanomagnetometry using shallow nitrogen vacancy centers, Nano Lett. **15,** 165 (2014).

[50] T. Häberle, T. Oeckinghaus, D. Schmid-Lorch, M. Pfender, F. F. de Oliveira, S. A. Momenzadeh, A. Finkler, and J. Wrachtrup, Nuclear quantum-assisted magnetometer, Rev. Sci. Instrum. **88,** 013702 (2017).

[51] T. Rosskopf, J. Zopes, J. M. Boss, and C. L. Degen, A quantum spectrum analyzer enhanced by a nuclear spin memory, npj Quantum Inf. **3,** 33 (2016).

[52] S. Yang, Y. Wang, D. D. B. Rao, T. H. Tran, A. S. Momenzadeh, M. Markham, D. J. Twitchen, P. Wang, W. Yang, R. Stöhr, P. Neumann, H. Kosaka, and J. Wrachtrup, High-fidelity transfer and storage of photon states in a single nuclear spin, Nat. Photonics **10,** 507 (2016).

[53] H. Zheng, J. Xu, G. Z. Iwata, T. Lenz, J. Michl, B. Yavkin, K. Nakamura, H. Sumiya, T. Ohshima, J. Isoya, J. Wrachtrup, A. Wickenbrock, and D. Budker, Zero-Field Magnetometry Based on Nitrogen-Vacancy Ensembles in Diamond, Phys. Rev. Appl. **11,** 064068 (2019).

[54] D. D. Bhaktavatsala Rao, S. Yang, S. Jesenski, E. Tekin, F. Kaiser, and J. Wrachtrup, Observation of nonclassical measurement statistics induced by a coherent spin environment, Phys. Rev. A **100,** 022307 (2019).